Chemical Science

ROYAL SOCIETY OF CHEMISTRY

EDGE ARTICLE

View Article Online
View Journal | View Issue

Cite this: *Chem. Sci.*, 2025, **16**, 5223

All publication charges for this article have been paid for by the Royal Society of Chemistry

Received 28th June 2024
Accepted 4th February 2025

DOI: 10.1039/d4sc04272g

rsc.li/chemical-science

1,4-Dihydropyrrolo[3,2-*b*]pyrrole modified with dibenzoxazepine: a highly efficient core for charge-transfer-based OLED emitters†

Krzysztof Górski,[a] Steve Shelton,[b] Jaijanarthanan Lingagouder,[c] Przemyslaw Data,*[c] Denis Jacquemin *[de] and Daniel T. Gryko *[a]

The present work is focused on designing novel heteroaromatic systems, formally a hybrid of dibenzo[*b*,*f*]oxazepines and 1,4-dihydropyrrolo[3,2-*b*]pyrroles (DHPPs). Straightforward synthesis affords a family of rigid, centrosymmetric, π-expanded aromatic heterocycles amenable to facile post-functionalization. The rigidified molecular architecture is responsible for several key photophysical features including (1) the excellent blue colour purity (full width at half maximum parameter = 0.435 eV) and (2) stronger emission compared to analogous DHPPs capable of free rotation. Comparison of dyes possessing nitro groups at various positions reveals that if NO_2 groups are located at distant positions the quadrupolar dye shows strong yellow fluorescence in non-polar solvents, whereas the same group at position 3 *versus* the DHPP core leads to a poorly emitting dye. Computational studies suggest that the key difference lies in relative energies of dark and bright excited states. It was shown that the DHPP core offers unique advantages as a high-emission energy system, serving as a foundation for charge-transfer (CT)-based efficient emitters. These features, combined with the ability to modulate electronic properties *via* peripheral functionalization, highlight the potential of the DHPP core in advanced optoelectronic devices, including new-generation OLEDs.

Introduction

Since the first synthesis of [7]circulene in 1983 by Yamamoto,[1] numerous developments have taken place in the physicochemistry of nonalternant π-extended systems. The distortion induced by the presence of a nonhexagonal ring leads to unusual molecular architectures[2–6] often possessing unique physicochemical properties such as specific supramolecular organization,[7] open-shell character,[8] or chiroptical activity.[9–11] An equally important way of modifying physicochemical properties is heteroatom displacement, which also allows modulation of the electronic structure.[12–15] However, due to the limited possibilities of the heteroatom incorporation into π-expanded nanographenes, this approach is not widely used in the chemistry of nonalternant π-extended dyes.[16–18]

The goal of this study was to expand the chemical space of large nonalternant π-conjugated architectures employing the unique possibilities offered by 1,4-dihydropyrrolo[3,2-*b*]pyrroles (DHPPs). DHPPs are a family of electron-rich heterocycles[19] exhibiting a variety of interesting properties such as solvatofluorochromism,[20] two-photon absorption,[21] and aggregation-induced emission.[22–24] For this reason, they have found many applications, including H-binding probes,[25] photochromic sensors,[26] mitochondria imaging fluorescent dyes,[27] solar cells,[28,29] and OLEDs.[30,31] Their popularity results from straightforward synthesis from readily available aldehydes and amines, which *in situ* form the corresponding imine, taking part in a further multicomponent process.[32] This reaction is one of the very few processes that (a) involves five molecules and (b) leads to a centrosymmetric aromatic heterocycle. This unique feature enables a quick build-up of molecular complexity.[33–35]

To this end, we resolved to use dibenzo[*b*,*f*]oxazepines, consisting of two peripheral benzene rings and a central 7-membered ring, in which oxygen and nitrogen atoms are incorporated. In our concept, dibenzo[*b*,*f*]oxazepine serves as a source of nonalternancy. Currently, many synthetic pathways leading to this heterocyclic system are known; however, the

[a]*Institute of Organic Chemistry, Polish Academy of Sciences, Kasprzaka 44/52, 01-224 Warsaw, Poland*
[b]*The Molecular Foundry, Lawrence Berkeley National Laboratory, Berkeley, CA 94720, USA*
[c]*Department of Molecular Physics, Faculty of Chemistry, Lodz University of Technology, 90-543 Lodz, Poland*
[d]*Nantes Université, CNRS, CEISAM UMR 6230, F-44000 Nantes, France. E-mail: Denis.Jacquemin@univ-nantes.fr*
[e]*Institut Universitaire de France (IUF), F-75005 Paris, France*

† Electronic supplementary information (ESI) available: Synthetic procedures, NMR spectra, UV-Vis spectra, cyclic voltammograms, OLED fabrication details and characteristics, computational details, Cartesian coordinates of ground and excited states, and X-ray structure details. CCDC 2364052 (**2e**). For ESI and crystallographic data in CIF or other electronic format see DOI: https://doi.org/10.1039/d4sc04272g

simplest approach is based on cross-condensation between commercially available 2-fluoro- or 2-chlorobenzaldehyde and the corresponding 2-hydroxyanilines.[36–41] Another important route toward constructing a heterocyclic 7-membered ring is an intramolecular, Vilsmeier-type reaction.[42] Nevertheless, modern chemical development did not omit the methodology of dibenzo[*b*,*f*]oxazepine synthesis, which can be obtained in the presence of a Pd-based catalyst.[43,44] While many dibenzo[*b*,*f*]oxazepine derivatives exhibit potential bioactivity and can act as pharmaceuticals,[45–50] data regarding their use in functional materials chemistry are, unfortunately, lacking.

Herein, we present a straightforward synthetic methodology leading to complex, nonalternant multiheteroatom nanographenes from readily available cyclic imines, namely dibenzo[*b*,*f*]oxazepines. π-Extended 1,4-dihydropyrrolo[3,2-*b*]pyrrole and dibenzo[*b*,*f*]oxazepine hybrids exhibit reversible oxidation and large fluorescence quantum yields exceeding 80%. Moreover, the peripheral modification of the parent electron-rich core with electron-accepting subunits results in dyes exhibiting near-infrared (NIR) emission. In this study, compound **2a** was chosen as a model emitter due to its high fluorescence quantum yield and excellent colour purity. This work highlights the synthesis, photophysical characteristics, and device performance of DHPP derivatives, emphasizing their potential as high-efficiency cores for CT emitters.

Results and discussion

Synthesis

Our strategy towards DHPPs bearing two dibenzo[*b*,*f*]oxazepine scaffolds relied on utilizing parent dibenzo[*b*,*f*]oxazepine (**1a**), as a cyclic imine, in our multicomponent reaction and exploiting typical imine reactivity, *via* the Mannich reaction.[51] The choice of this approach relies on the proven fact that Schiff base formation is the first step in the formation of DHPPs. At the same time, we underline that cyclic imines were never used in this reaction and our earlier attempts to employ phenanthridine failed. The model reaction with **1a** carried out under standard conditions[32] led to the formation of desired DHPP **2a**, with, however, a small yield of 3.6% (Table 1, entry 1). Notably, the formation of **2a** seems to be much faster than typical 1,4-dihydropyrrolo[3,2-*b*]pyrrole prepared from acyclic imines, which may be related to the *Z* configuration of the double bond in **1a**. Nevertheless, changing the solvent system (Table 1, entry 2) or the acidity of the reaction environment (Table 1, entry 4) was ineffective for increasing the yield of the desired product. Moreover, even utilizing conditions under which substrate **1a** undergoes the Mannich reaction[51] doesn't affect the reaction course toward the formation of DHPP **2a** (Table 1, entry 5).

An aspect that needs to be taken into account is the intrinsic electron-rich character of the central 1,4-dihydropyrrolo[3,2-*b*]pyrrole core, which is enhanced in dye **2a**, due to the partial planarization of peripheral substituents leading to increased conjugation over the entire molecule (see calculations below). Thus, the presence of an oxidant, such as $Fe(ClO_4)_3$, which is necessary under standard 1,4-dihydropyrrolo[3,2-*b*]pyrrole synthesis conditions,[32] in this case, may enhance the decomposition of dye **2a**. Thus, we decided to exclude $Fe(ClO_4)_3$, returning to the initially published conditions.[52] The reaction time however was prolonged up to 48 h and the whole process required the addition of another portion of butane-2,3-dione after 24 h, which resulted in a slight increase in the yield of product **2a** (Table 1, entry 3). Gratifyingly, increasing four times the amount of butane-2,3-dione simultaneously with increasing the reaction temperature up to 80 °C led to a sharp increase in the reaction yield to ≈6% (Table 1, entry 6). Further changes in the reaction conditions did not lead to any improvements (Table 1, entry 7 and 8). Having suitable reaction conditions in

Table 1 Optimisation of reaction conditions (scale 2 mmol of **1a**)

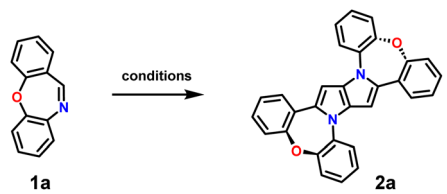

1a **2a**

Entry	Conditions	*T* [°C]	*t* [h]	Yield [%]
1	1 ml AcOH, 1 ml toluene, butanedione (1 mmol), $Fe(ClO_4)_3$ (3% mol)	50	24	3.6
2	1 ml AcOH, butanedione (1 mmol), $Fe(ClO_4)_3$ (3% mol)	50	24	2.2
3	1 ml AcOH, butanedione (1 mmol), after 24 h additional butanedione (1 mmol)	50	48	4.2
4	1 ml AcOH, 1 ml toluene, 1 ml 1,2-dichloroethane, butanedione (1 mmol), CH_3SO_3H (0.1 mmol), $Fe(ClO_4)_3$ (3% mol)	50	24	0.0
5	1 ml AcOH, 6 ml DMSO, butanedione (1 mmol), L-proline (0.6 mmol), $Fe(ClO_4)_3$ (3% mol)	50	24	0.0
6	**2 ml AcOH, 2 ml toluene, butanedione (4 mmol)**	**80**	**24**	**6.0**
7	2 ml AcOH, 2 ml toluene, butanedione (1 mmol)	40	72	3.1
8	2 ml AcOH, 2 ml toluene, butanedione (4 mmol)	100	24	3.0

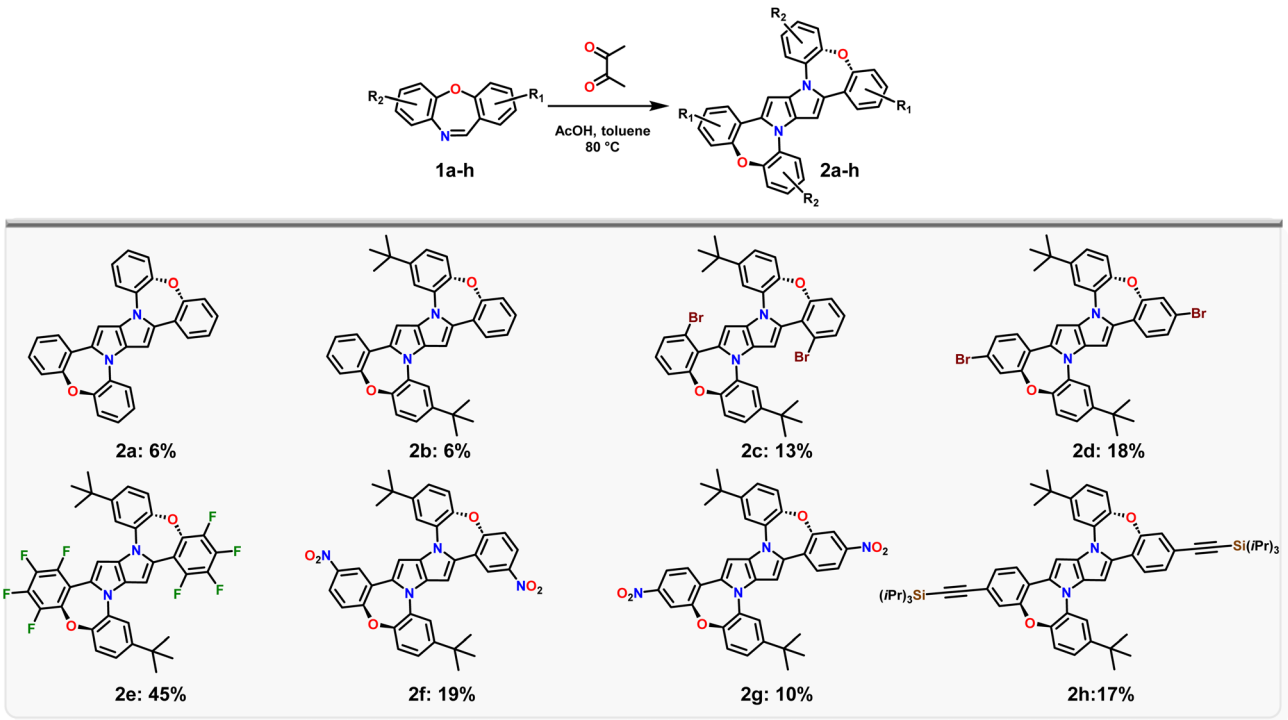

Scheme 1 The scope of dibenzo[*b*,*f*]oxazepines able to form 1,4-dihydropyrrolo[3,2-*b*]pyrroles (**2a–g**).

hand we resolved to probe the scope of this reaction to embrace electron-withdrawing substituents such as bromine atoms potentially opening the pathway towards larger architectures *via* post-functionalization. Thus we investigated the scope of dibenzo[*b*,*f*]oxazepines able to form 1,4-dihydro-pyrrolo[3,2-*b*] pyrroles (Scheme 1). The introduction of an alkyl chain, such as *t*-butyl, doesn't affect the reaction yield (**2b** – 6%), whilst, using brominated dibenzo[*b*,*f*]oxazepines **1c, d** distinctly increases the reaction yield (**2c** – 13% and **2d** – 18%). This rather unusual result is plausibly a direct consequence of the decreased solubility of **2c** and **2d**, caused by the presence of bromine atoms (a smaller amount of the desired product is prone to oxygen-promoted decomposition). A perfect illustration of this effect is the transformation of **1e** into **2e**, which occurs with 45% yield. Interestingly, for dibenzo[*b*,*f*]oxazepines containing a nitro group (**1f, g**) or a tri-i-propylsilyl protected acetylene (**1h**), the formation of the corresponding 1,4-dihydro-pyrrolo[3,2-*b*] pyrroles **2f–h** ranges from 10% to 19%.

Having in our hands a panel of DHPPs bearing two dibenzo [*b*,*f*]oxazepine units, we embarked on their post-functionalisation. Since the most interesting photophysical effects in DHPPs were found in centrosymmetric quadrupolar A–D–A architectures,[19,20] the general post-functionalization strategy was directed towards attaching electron-deficient units at peripheral positions of the new core. Dye **2d** when heated in *N*-methylpyrrolidone in the presence of CuCN undergoes conversion into mono- and dicyanoderivatives **3a, b** (Scheme 2). DHPPs possessing cyano groups but in different arrangements were obtained *via* a Suzuki reaction with 4-cyanophenylboronic acid, resulting in the formation of **4a, b** with moderate yields. On the other hand, dye **2h** under sila-Sonogashira reaction conditions[53] can be directly transformed into elongated donor–acceptor architectures **5a–d**, in which the electron-rich 1,4-dihydro-pyrrolo[3,2-*b*]pyrrole core is peripherally decorated with acceptor subunits such as nitrile (DHPP **5a**), 5-thiatruxene sulfone (DHPP **5b**),[54] naphthalimide (DHPP **5c**) or perylenediimide (DHPP **5d**) (Scheme 3).

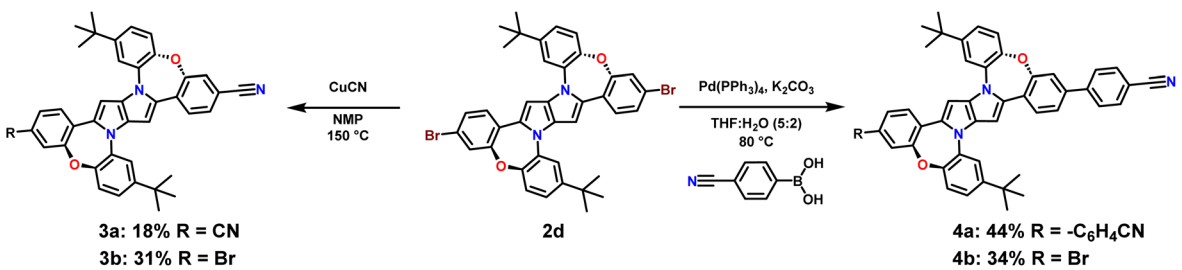

Scheme 2 Post-functionalization of DHPP **2d**.

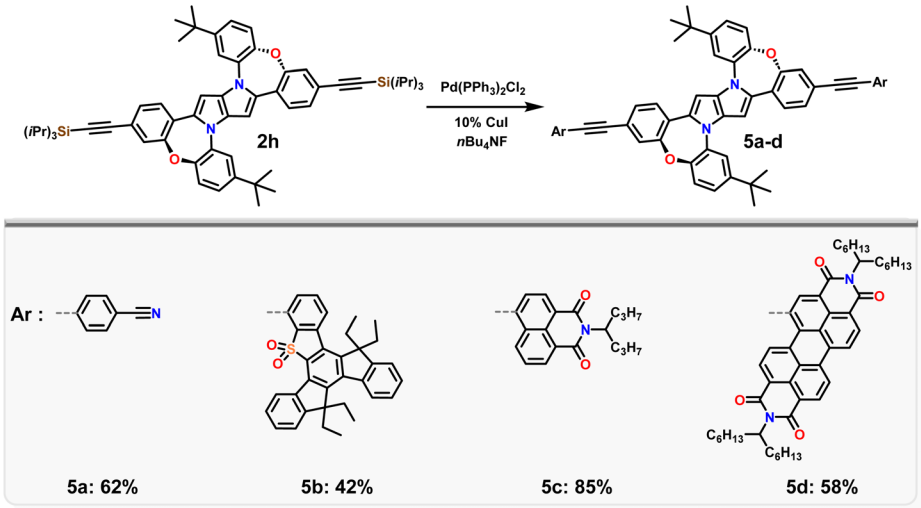

Scheme 3 Post-functionalization of DHPP **2h** *via* the sila-Sonogashira protocol.

Crystal structure

While most of the obtained dyes tend to crystalize, only **2e** provided X-ray quality crystals. As shown in Fig. 1a and c, the molecule consists of a planar DHPP-based centre, decorated peripherally with a dibenzo[*b*,*f*]oxazepine subunit, characteristically bending the molecule around an oxygen atom with a distortion angle of about 126°. While many π-expanded dyes suffer from low solubility, this deformation acts oppositely; thus, **2e** exhibits sufficient solubility in most non-polar and moderately polar solvents. DFT calculations suggest that the obtained dyes can exist in two major forms: C_i-centrosymmetric and C_2-symmetric, with the molecule containing an inversion center being *ca.* 0.42 kcal mol^{-1} more stable. This is consistent with the **2e** structures, which crystallize in the $P\bar{1}$ space group, though we cannot exclude a mixture of both forms in solution.

Distortion within the 7-membered ring (Fig. 1c) hinders strong π-stacking; however, fluorinated rings tend to interact (d = 3.410 Å), leading to aggregates within the entire crystal lattice (Fig. 1b and d). Consequently, new hybrids of 1,4-dihydropyrrolo[3,2-*b*]pyrrole with dibenzo[*b*,*f*]oxazepine can be considered potential semiconductors. Furthermore, strong association modifies the electronic structure; thus, the described intermolecular interactions are directly responsible for the distinct changes of spectroscopic properties observed during passing from solution to solid, in the synthesized dyes.

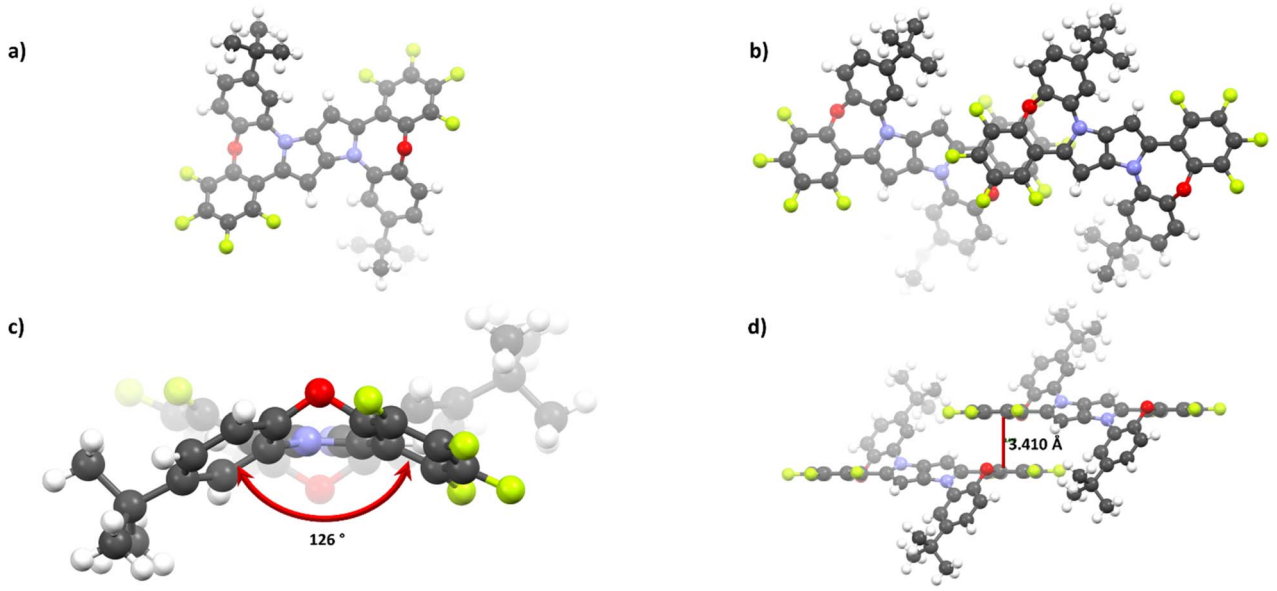

Fig. 1 X-ray structure of **2e**, (a) single molecule – top view, (b) interaction between two molecules – top view, (c) single molecule – side view, and (d) interaction between two molecules – side view. Depth hue was used to present the spatial orientation of atoms in the molecule and crystal lattice.

Table 2 Absorption and emission data for the synthesized dyes in solution (non-bold – toluene and bold – dichloromethane)[a]

Dye	λ_{abs}^{max} [nm] ($\varepsilon/10^3$ [M^{-1} cm^{-1}])	λ_{em}^{max} [nm]	$\Delta\nu$ [cm^{-1}]	Φ_{fl} [%]
2a	363 (33.2), 375 (31.6)	407, 424	2100	80
	361 (37.0), 372 (35.0)	**407, 424**	**2300**	**69**
2b	362 (41.2), 373 (39.4)	410, 425	2400	69
	361 (39.1), 371 (37.0)	**410, 425**	**2600**	**69**
2c	369 (38.4), 382 (36.6)	425	2600	0.1
	366 (34.8), 376 (33.1)	**421**	**2800**	**0.07**
2d	372 (45.5), 383 (44.0)	421, 437	2400	15
	372 (47.1), 383 (45.2)	**421, 437**	**2400**	**5**
2e	358 (44.9), 374 (43.7)	404, 419	2000	64
	357 (21.6), 371 (20.6)	**404, 419**	**2200**	**28**
2f	371 (33.5)	629	11 100	2
	370 (40.8)	—	—	—
2g	465 (39.0)	572	4000	93
	477 (47.0)	**716**	**7000**	**6**
2h	402 (69.9), 420 (71.2)	450, 474	1600	82
	401 (69.9), 413 (69.3)	**453, 474**	**2100**	**85**
3a	404 (27.5), 421 (29.1)	451, 474	1600	87
	409 (33.3), 421 (34.4)	**460, 480**	**2000**	**86**
4a	418 (29.7)	484, 506	3300	90
	417 (33.6)	**531**	**5100**	**95**
5a	434 (57.3)	494, 517	2800	100
	435 (72.1)	**544**	**4600**	**96**
5b	376 (26.7), 456 (68.4)	504, 531	2100	79
	380 (33.1), 449 (79.8)	**555**	**4200**	**81**
5c	377 (40.4), 475 (54.7)	581	3800	77
	377 (47.3), 474 (63.4)	**793**	**8500**	**1**
5d	532 (94.3), 611 (26.4)	836	4400	<0.001
	530 (88.5), 591 (26.1)	—	—	—

[a] λ_{abs}^{max} – absorption maximum wavelength, ε – molar absorption coefficient, λ_{em}^{max} – emission maximum wavelength, $\Delta\nu$ – Stokes shift, Φ_{fl} – fluorescence quantum yield. 9,10-Diphenylanthracene in toluene was used as the quantum yield standard (Φ_{fl} = 70%).

Experimental and theoretical spectroscopic studies

The unsubstituted parent heterocycle **2a** and its alkyl derivative **2b** and halogenated derivatives **2c–e** exhibit strong absorption with a λ_{abs}^{max} around 375–382 nm in toluene (Table 2, Fig. 2 and S52–S56†), which corresponds to a $S_0 \rightarrow S_1$ transition characterized by high oscillator strengths exceeding 1 according to TD-DFT calculations (Table S1†). Nevertheless, in the case of dye **2e**, using dichloromethane induces a nearly twofold drop in the observed absorption molecular coefficient (ε). Similar behaviour was also noticed in some 4,5,6,7-tetrafluorobenzo[*b*]furane derivatives.[55] On the other hand, a small expansion of the π-electron system caused by the introduction of two (tri-i-propylsilyl)acetylene moieties (dye **2h**) distinctly changes the absorption spectrum. First of all, it is bathochromically shifted by about 2800 cm^{-1} (Table 2), in both solvents in comparison to DHPP **2a**. Secondly, an enormous oscillator strength ($f \approx 2$, Table S1†) is computed for the $S_0 \rightarrow S_1$ electron transition, consistent with the observed near doubling of the ε which reaches about 71 000 M^{-1} cm^{-1}.

However, the lack of essential changes in the absorption spectra upon solvent polarity increasing, for compounds **2a–e** and **2h**, indicates a centrosymmetric molecular structure, which is in line with the X-ray results as well as DFT results.

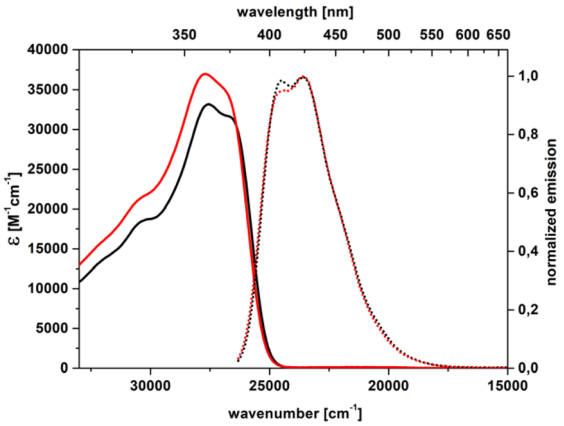

Fig. 2 Absorption (solid) and emission (dot) spectra of **2a** in toluene (black) and dichloromethane (red).

For dyes **2a–e**, the fluorescence appears in the blue region, with λ_{em}^{max} ranging around 407 nm to 425 nm (Table 2). The fluorescence of dye **2a** characterized by the particular purity of the blue emission (CIE 1931: 0.156; 0.032) and large fluorescence quantum yield (Φ_{fl}) reaching 80% in toluene deserves special attention. On comparing the electron density difference (EDD) plots of **2a** to that of its unbridged counterpart, *i.e.* 1,2,4,5-tetraphenyl-1,4-dihydropyrrolo[3,2-*b*]pyrrole, one notices quite similar topologies (Fig. 3). Nevertheless, the Φ_{fl} in toluene for the former is more than twice that of the latter.[52] Undoubtedly, the observed differences have to be related to more effective nonradiative dissipation of energy in the excited state in the case of 1,2,4,5-tetraphenyl-1,4-dihydropyrrolo[3,2-*b*]pyrrole compared with DHPP **2a**. Analyses of the S_0 and S_1 geometries for both molecules reveal that the relaxation of 1,2,4,5-tetraphenyl-1,4-dihydropyrrolo[3,2-*b*]pyrrole in the S_1 state involves rotation of the benzene rings attached to positions 2 and 5 by *ca.* 20°, while in **2a** planarization of the entire molecule is observed, yet with smaller changes in the dihedral angle, consistent with an increased emission yield (Fig. 3). This improved rigidity may also explain the excellent blue colour purity which is directly correlated with a rather narrow full width at half maximum parameter (FWHM = 0.435 eV). Consistently, a comparison of the photophysics of dye **2a** and 2,5-bis(2-methoxyphenyl)-1,4-bis(4-methylphenyl)-1,4-dihydropyrrolo[3,2-*b*]pyrrole[56] indicates that the λ_{abs}^{max} of **2a** is bathochromically shifted by *ca.* 30 nm in CH_2Cl_2 whereas the λ_{em}^{max} values are essentially the same.

As stated above, the optical spectra of dyes **2a–e** are also rather equivalent. This is consistent with the fact that the EDD involved in $S_0 \rightarrow S_1$ and in $S_1 \rightarrow S_0$ transitions are located on the same part of the molecules **2a–e** (Fig. S82†). Dye **2h** differs somewhat, in which the excited-state reorganization also partially involves the (tri-i-propylsilyl)acetylene subunits that act as weak electron acceptors (Fig. S82†), consistent with the observed redshifts (Table 2). However, no distinct solvatofluorochromism is found.

Nevertheless, while the introduction of a *t*-butyl group (**2b**) does not significantly impact either λ_{em}^{max} or Φ_{fl} (Table 2), the

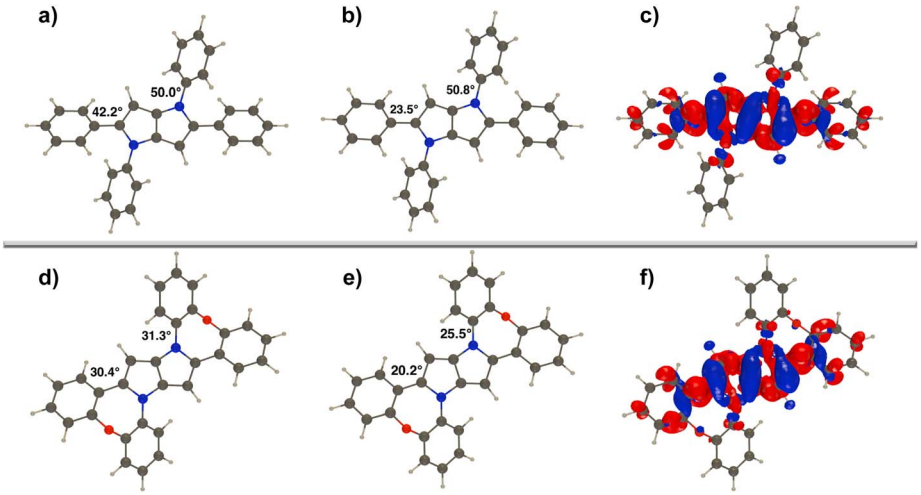

Fig. 3 Optimal ground (a) and excited state (b) structures of 1,2,4,5-tetraphenyl-1,4-dihydropyrrolo[3,2-*b*]pyrrole with key dihedral angles represented, together with the EDD plot (c). Optimal ground (d) and excited state (e) structures of **2a** with key dihedral angles represented, together with the EDD plot (f). In the EDD plots, the blue and red lobes correspond to a decrease and increase in electron density, respectively. The contour threshold is 0.001.

presence of bromine atoms in **2c, d** leads to a significant drop of Φ_{fl} in toluene, to 0.1% and 15%, and in dichloromethane to 0.07% and 5%, respectively. While the lowering of the fluorescence quantum yield can be easily explained by an increased population of triplet states (intersystem crossing), caused by the heavy atom effect, distinct differences between Φ_{fl} for **2c** and **2d** suggest the presence of another nonradiative relaxation channel of the S_1 state for **2c**. Indeed, ^{1}H NMR spectra of dye **2c**, recorded at different temperatures, indicate that the presence of bromine atoms raises the energy barrier between the C_i and C_2 conformations (Fig. S23†), which might explain the different photophysical behaviour of the two compounds. Unlike **2a–d**, the fluorescence of **2h** is distinctly bathochromically shifted to ≈450 nm, for both solvents (Table 2); nevertheless, the redshift of the emission doesn't affect Φ_{fl}, which ranges around 82%.

The enhanced electron-donating character of the new heterocyclic core in DHPP **2a** opened the pathway for exploring the photophysics for derivatives possessing two peripheral electron-accepting subunits. The first class of such systems is nitro-aromatics **2f, g**. The nitro group in **2f** slightly influences the absorption, practically not changing the λ_{abs}^{max}, compared to **2a** (Table 2). On the other hand, the effect of the NO_2 moiety in the case of **2g** is much more pronounced, shifting the λ_{abs}^{max} by about 100 nm toward lower energy. Such changes are qualitatively reproduced by theory (Table S1†). Despite the acceptor–donor–acceptor structure of dyes **2f, g**, no changes in absorption spectra are observed upon solvent polarity increasing (Fig. S57 and S58†), indicating the centrosymmetric quadrupolar character of these nitro-aromatics.[57] The NO_2 group is strongly involved in the $S_0 \rightarrow S_1$ excitation process (Fig. S82†), causing the relocation of electron density from the center of the molecule toward the electron-deficient moiety. Dye **2g** exhibits both strong fluorescence in toluene in the yellow region and strong solvatofluorochromism indicating excited-state symmetry breaking[58–60] (Table 2). Indeed, upon increasing solvent polarity, the emission spectrum becomes dramatically redshifted (λ_{em}^{max} = 716 nm in DCM *versus* λ_{em}^{max} = 572 nm in toluene) with a simultaneous, nearly 16-times decrease in fluorescence quantum yield. In contrast, the emission spectrum of **2f** is extremely redshifted, with $\Delta\nu$ = reaching 11 000 cm^{-1} in toluene, while for **2g** it is only 4000 cm^{-1}. This behaviour is directly related to charge delocalization at the S_1 state. In both compounds the first electron excitation possesses a distinct charge transfer character; however, the mutual orientation of the 1,4-dihydropyrrolo[3,2-*b*]pyrrole core and the NO_2 group in **2g** leads to significant delocalization, while in the case of **2f**, the charge becomes more localized. In toluene, the Φ_{fl} values are markedly different for these two dyes (2% for **2f** and 93% for **2g**). This effect could be rationalized using theory, since in **2f** there are two nearly degenerated states (one bright and one dark) and the fluorescence is likely quenched by the presence of this dark state, whereas in **2g**, the dark state is significantly shifted up in energy and plays no role in the photophysics.[61] In the context of fluorescent nitroaromatics, it is interesting to compare **2f** and **2g** to their analogs lacking rigidification imparted by dibenzoxazepine.[62] Whereas λ_{abs}^{max} and λ_{em}^{max} of 2,5-bis(4-nitrophenyl)-1,4-dihydropyrrolo[3,2-*b*]pyrrole and 2,5-bis(3-nitrophenyl)-1,4-dihydropyrrolo[3,2-*b*]pyrrole are located at almost the same wavelengths as those of dyes **2f** and **2g**, the emission intensity is enhanced after rigidification of the structure. In particular in the case of dye **2f** the Φ_{fl} is 10 times higher than that of 2,5-bis(3-nitrophenyl)-1,4-dihydropyrrolo[3,2-*b*]pyrrole in toluene.

A more typical picture for the behaviour of quadrupolar, centrosymmetric dyes presents a series of nitrile derivatives **3a**, **4a** and **5a**, which structurally differ from each other in the distance between the electron-withdrawing CN group and electron-rich core. In comparison to dye **2a**, the absorption spectra of all nitrile derivatives are significantly bathochromically shifted, while the absorption maximum increases along with donor–acceptor separator length, reaching 434 nm for **5a** (Table 2). As in other discussed systems, first electron excitation mostly involves the 1,4-dihydropyrrolo[3,2-*b*]pyrrole core;

however, in the series of **3a** → **4a** → **5a**, a distinct rearrangement of electron density toward the accepting moiety is observed (Fig. S82 and S83†). While ε values for **3a** and **4a** at the λ_{abs}^{max} range from 29 × 10^3 M^{-1} cm^{-1} to 34 × 10^3 M^{-1} cm^{-1}, elongation of the donor–acceptor separator by the introduction of the triple bond increases ε more than twice, in the case of **5a** (Table 2). Moreover, similar changes, as observed in **2h**, are also found in dyes **5b–d**; thus ε increasing can be directly related to π-electron expansion, caused by the presence of carbon–carbon triple bonds. Despite some differences in ε values, solvent polarity increasing slightly affects absorption spectra of **3a**, **4a** and **5a–d**. On the other hand, distinct changes are observed in the emissive properties of nitrile derivatives. While **3a**, **4a** and **5a** exhibit pronounced solvatofluorochromism, the strongest response to the increasing solvent dielectric constant is observed for DHPP **5a** (Table 2 and Fig. S60–S62†). A larger distance between the DHPP core and electron-accepting moieties leads to more pronounced charge separation upon excitation, making the $S_1 \rightarrow S_0$ transition energy noticeably smaller. Nevertheless, for all nitrile derivatives in both solvents, a large Φ_{fl} is maintained, ranging between 90 and 100% (Table 2). Similar to previously described nitroderivatives, rigidification slightly affects λ_{abs}^{max} and λ_{em}^{max} when comparing **5a** to corresponding unbridged 1,4-dihydropyrrolo[3,2-*b*]pyrrole;[63] however, Φ_{fl} of **5a** is nearly 5 times higher.

Replacing the 4-cyanophenyl substituent with stronger electron-accepting subunits, such as 5-thiatruxene sulfone (**5b**),[64] naphthalimide (**5c**), or perylenediimide (**5d**), leads to an even more pronounced bathochromic shift of λ_{abs}^{max} reaching 611 nm for **5d** (Table 2, Fig. 4 and S63–S65†). Similarly to nitrile derivatives, the EDD plots corresponding to an $S_0 \rightarrow S_1$ excitation in **5b** show that the electronic reorganization takes place in the molecule's center, with distinct displacement toward the sulfone groups (Fig. S83†). Moreover, by increasing the electron-accepting character of the electron-withdrawing moiety (**5c and d**), the charge-transfer character becomes more pronounced. The visible solvatofluorochromic response of **5b** is accompanied by maintaining a large Φ_{fl} of about 80%, for both solvents (Table 2). The strong fluorescence redshifts observed for **5c** and **5d**, with λ_{em}^{max} = 793 nm and 836 nm, respectively, with a fluorescence tail reaching >1100 nm, clearly show NIR emission (Fig. S63 and S64†). However, such a lowering of the $S_1 \rightarrow S_0$ energy band gap increases the efficiency of the nonradiative deactivation of the excited S_1 state (according to the so-called energy gap law), and the values of Φ_{fl} become rather small (Table 2).

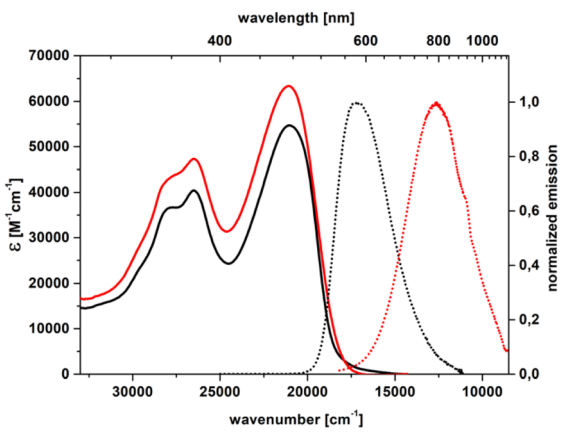

Fig. 4 Absorption (solid) and emission (dot) spectra of **5c** in toluene (black) and dichloromethane (red).

Photostability and thermal stability

Due to **2a** representing a new class of nonalternant multiheteroatom doped nanographenes and single photon spectroscopy revealing interesting properties of this system and its derivatives, we decided to estimate the photostability of **2a** by quantitatively determining the photodegradation quantum yield (Φ_{deg}). To this end, we used an already well-established protocol,[65] that considers both the range of light inducing the decay and the absorption spectrum of the compound, which is not often the case in the literature. Irradiation was performed in an aerated toluene solution at around 20 °C. Absorption spectra were recorded at intervals of 60 seconds, during which time the solution was exposed to 363 nm light, which was sufficient to observe clear changes (Fig. S66a†). Moreover, the linear course of the $A_0/A(t)$ relationship as a function of $F(t)$ indicates the lack of absorption bands of the photodecomposition product and allows the determination of the slope coefficient necessary to calculate the photodegradation quantum yield (Fig. S66b†). Φ_{deg} was estimated to be *ca.* 0.014%, corresponding to the photodecomposition of one molecule upon absorption of around 7200 photons, which stands in line with the electron-rich nature of **2a**.

To evaluate the thermal properties of **2a** thermogravimetry analysis (TGA) and differential scanning calorimetry (DSC) measurements were performed under a nitrogen atmosphere. TGA reveals significant changes in sample mass, around 10%, in the range of 360 to 400 °C (Fig. S85a†). On the other hand, DSC shows the endothermic process with a peak of 395 °C corresponding to the melting point (Fig. S85b†). Thus mass drop is correlated to slow evaporation of the sample rather than decomposition, indicating high thermal stability of **2a**. Interestingly, two different exothermic processes can be observed at 262 °C and 202 °C upon cooling (Fig. S86†). The significant difference between the melting point and overcooled recrystallization process (133 °C) indicates difficulties related to the appropriate orientation of molecules within the forming crystal lattice, likely related to distortions caused by the 7-membered ring hindering strong intermolecular interactions. On the other hand, the process appearing at 202 °C is probably correlated to reorganization within the crystal lattice formed at 262 °C, leading to other crystalline structure. Confirmation of this assumption can be found during the analysis of the next heating cycle which reveals changes in the melting point (382 °C). The broad peak at 382 °C suggests inhomogeneity of the crystalline structure formed at 202 °C, while the difference in the melting point between the first heating cycle and the second one (13 °C) points to significant changes in the crystalline structure.

Table 3 Redox properties of novel DHPPs[a]

Dye	$E_{1/2}^{ox}$ [V]	E_{HOMO} [eV]	ΔE_{opt} [eV]	E_{LUMO} [eV]
2a	0.71	−5.51	3.17	−2.34
2b	0.72	−5.52	3.17	−2.35
2c	0.82	−5.62	3.07	−2.55
2d	0.73	−5.53	3.08	−2.45
2e	1.00	−5.80	3.19	−2.61
2f	0.98	−5.78	2.92*	−2.86
2g	0.34	−5.14	2.39	−2.75
2h	0.72	−5.52	2.85	−2.67
	0.83	−5.63		
3a	0.91	−5.71	2.84	−2.87
4a	0.80	−5.60	2.75	−2.85
5a	0.74	−5.54	2.67	−2.87
5b	0.27	−5.07	2.58	−2.49
	0.72	−5.52		
5c	0.75	−5.55	2.35	−3.20
5d	0.25	−5.05	1.71	−3.34

[a] $E_{1/2}^{ox}$ – oxidation half-wave potential measured in dichloromethane *vs.* Fc/Fc^+, E_{HOMO} – the energy of the HOMO calculated from the first oxidation potential as $-e(4.8 + E_{1/2}^{ox})$, ΔE_{opt} – optical band gap in toluene, estimated from absorption and emission spectra cross-section (* – determined from absorption spectra onset), and E_{LUMO} – the energy of the LUMO estimated using $\Delta E_{opt} + E_{HOMO}$.

Electrochemistry

Anticipating their application in optoelectronic devices, we decided to study the electrochemical properties for all novel heterocyclic dyes using cyclic voltammetry. Indeed, the energy of the highest occupied molecular orbital (HOMO) and the reversibility of the redox process are particularly relevant parameters. All compounds exhibit a reversible first oxidation process, while a second oxidation can be observed in both **2h** and **5b** (Fig. S74 and S78†). Except for **2g** and **5b, d**, the first oxidation takes place in the 0.7 V to 1.0 V *vs.* the Fc/Fc^+ range. The determined $E_{HOMO} = -5.51$ eV of **2a** insignificantly changes upon attachment of an alkyl chain (**2b**), a bromine atom (**2d**) or (tri-i-propylsilyl)acetylene moieties (**2h**) (Table 3). However, the stabilization of the HOMO level for **2c** by *ca.* 0.1 eV indicates that some steric, as well as electronic effects, can modulate its energy. Nevertheless, the strongest stabilization is caused by the presence of 8 fluorine atoms (**2e**), logically inducing a lowering of the HOMO level by *ca.* 0.3 V as compared to **2a**, down to −5.80 eV.

On the other hand, a fascinating relation can be observed when quadrupolar dyes, **3a**, **4a** and **5a**, are compared. Increasing the distance between the electron-rich core and the accepting nitrile group in one-photon spectroscopy leads to a gradual redshift of the emission spectra (see above). Yet the direction of the impact of the CN moiety completely differs for the ground electronic state. Upon increasing the length between the donor and acceptor subunits, the HOMO undergoes significant destabilization, up to −5.54 eV for **5a**, which is only 0.03 eV lower than HOMO energy of the benchmark **2a** (Table 3). This indicates that, despite the conjugation between the electron-rich centre and the electron-withdrawing CN group, the influence of a nitrile moiety in the ground state is significantly weakened.

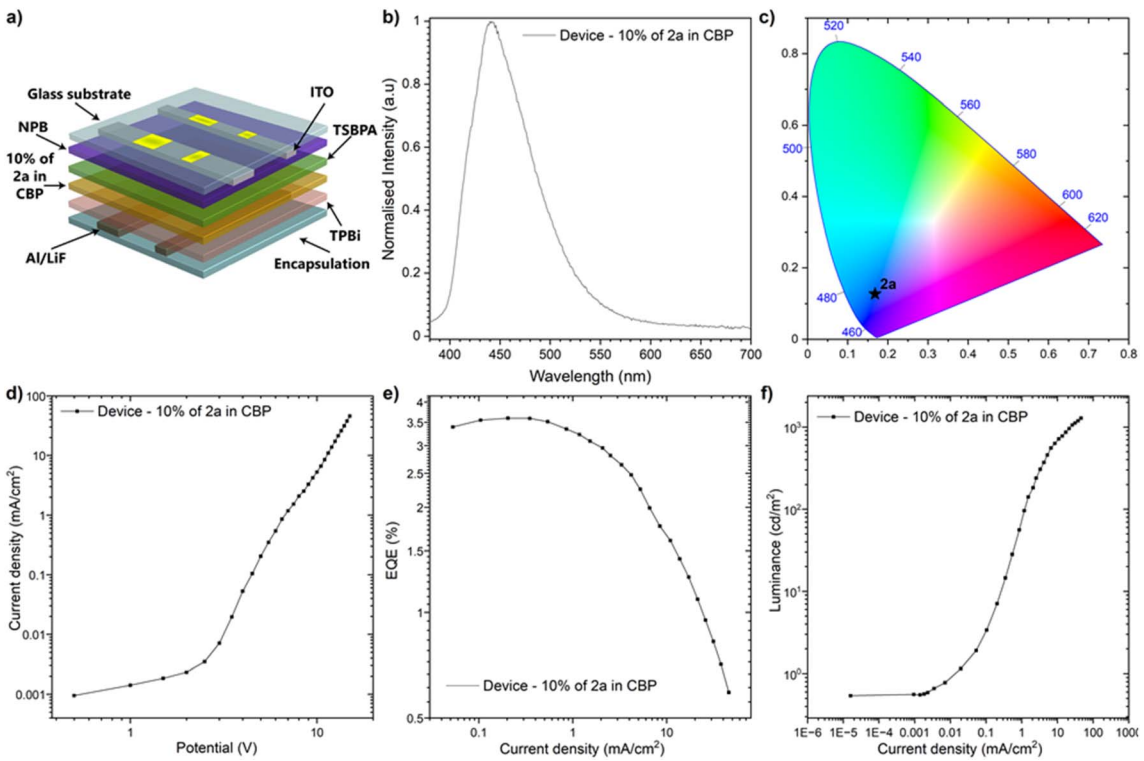

Fig. 5 OLED device characteristic: (a) schematic of an OLED device structure with a **2a** active layer, (b) electroluminescence spectrum of the studied device, (c) CIE 1931 chromaticity diagram indicating blue emission, (d) current density – potential, (e) external quantum efficiency-current density and (f) luminance-current density characteristics of the studied device.

Table 4 Electroluminescence data of the OLED device[a]

Device	Turn-on voltage [V]	λ_{em} [nm]	L_{max} [cd m^{-2}]	η_{max} [cd A^{-1}]	CIE coordinates (x, y)	EQE (%)		
						Max	100 cd m^{-2}	1000 cd m^{-2}
2a	3.5	440	1285	13.01	0.168, 0.127	3.59	3.21	1.02

[a] λ_{em} – emission wavelength, L_{max} – maximal luminance, η_{max} – current efficiency, and EQE – external quantum yield.

OLED device characteristics

To evaluate the applicability of the new compounds in optoelectronic devices,[66–72] OLEDS were fabricated and characterized. Compound **2a** was selected based on its favourable molecular design, characterized by a π-conjugated core integrating the dibenzo[*b*,*f*]oxazepine and 1,4-dihydropyrrolo[3,2-*b*]pyrrole frameworks. This hybrid structure confers high photophysical performance, including a large fluorescence quantum yield ($\Phi_{fl} \approx 80\%$) and excellent colour purity. The energy levels of compound **2a**, determined from electrochemical and spectroscopic studies, indicated compatibility with commonly used host materials, leading to the choice of CBP (4,4′-bis(*N*-carbazolyl)-1,1′-biphenyl) as the host. The device structure was designed carefully, considering energy alignment and charge transport properties. The optimized architecture comprised ITO (Indium Tin Oxide) as the anode for hole injection, NPB (*N*,*N*′-bis(naphthalene-1-yl)-*N*,*N*′-bis(phenyl)-benzidine) (30 nm) as the hole transport layer, TSBPA (4,4′-(diphenylsilanediyl) bis(*N*,*N*-diphenylaniline)) (10 nm) as a hole-blocking layer to confine excitons, 10% of compound **2a** in CBP (20 nm) as the emissive layer, TPBi (2,2′,2″-(1,3,5-benzinetriyl)-tris(1-phenyl-1-*H*-benzimidazole)) (50 nm) as the electron transport layer, and LiF (1 nm)/Al (100 nm) as the cathode. The device architecture, depicted in Fig. 5a, was inspired by previously reported designs but tailored to maximize the performance of the DHPP-based emitter. This multilayer structure ensured effective charge injection, recombination, and exciton confinement, key to achieving high efficiency. The fabricated OLEDs demonstrated excellent performance. The electroluminescence spectrum, shown in Fig. 5b, revealed a peak emission at 440 nm, corresponding to pure blue light. Nevertheless, the Commission Internationale de l'Éclairage (CIE) chromaticity coordinates (Fig. 5c) of the device ($x = 0.167$, $y = 0.127$) confirmed the high colour purity of the emission, a critical feature for display applications. The current density–voltage and luminance characteristics, presented in Fig. 5d and f, highlight the device's efficient charge injection and light output. The OLED exhibited a low turn-on voltage of approximately 3.5 V and reached a luminance peak of 1285 cd m^{-2}. These results underscore the suitability of compound **2a** for energy-efficient light-emitting applications. However, significant roll-off in luminance and efficiency was observed at higher current densities, likely caused by triplet–triplet annihilation or charge imbalance. The device's external quantum efficiency (EQE), as shown in Fig. 5e and Table 4, reached a maximum of 3.59%, validating the high emissive efficiency of compound **2a**. This performance is attributed to the molecular rigidity of **2a**, which reduces non-radiative decay and its optimal energy alignment with the CBP host. Furthermore, the planar and π-conjugated structure of **2a** facilitates effective charge transport and exciton generation, contributing to its high EQE. The design and performance of compound **2a** in the OLEDs are deeply rooted in its molecular structure. The dibenzo[*b*,*f*]oxazepine units introduce rigidity and prevent vibrational relaxation, while the central DHPP core contributes to its electron-donating properties. Combined with a well-matched host–guest energy alignment, these structural features result in efficient exciton formation and radiative recombination. Despite these successes, efficiency roll-off at voltages exceeding 9 V remains challenging, likely due to bimolecular quenching processes. Future work could address these issues by optimizing the layer thicknesses, introducing advanced host materials, or employing tandem architectures to mitigate exciton–polaron interactions.

Conclusions

We have proven for the first time that cyclic imines can be transformed into 1,4-dihydropyrrolo[3,2-*b*]pyrroles as long as imine functionality is not embedded into an aromatic core. The resulting electron-rich dyes possessing two dibenzo[*b*,*f*]oxazepine scaffolds fused with a DHPP core are rigid and more planar compared to typical tetraarylpyrrolo[3,2-*b*]pyrroles. Their unusual, curved yet rather rigid architecture is responsible for appreciable photophysical properties which include large fluorescence quantum yields exceeding 80% in almost all cases regardless of the substitution pattern. Moreover rigidification also results in more narrow emission spectra and higher colour purity for the non-substituted, parent blue-emitting dye. Moreover, peripheral functionalization with strong electron-accepting moieties bathochromically shifts emission toward the near-infrared region (NIR). The optoelectronic device performance results demonstrate the potential of compound **2a** as a highly efficient blue emitter for OLED applications. The combination of excellent photophysical properties, molecular stability, and device performance of this DHPP-based compound exemplifies its efficiency in blue emission and device compatibility, paving the way for novel OLED technologies. Future work will explore structural diversification to broaden the application scope of DHPP-based materials in optoelectronics.

Data availability

The data supporting the article entitled '1,4-Dihydropyrrolo[3,2-*b*]pyrrole modified with dibenzoxazepine: A Highly Efficient

Core for Charge-Transfer-Based OLED Emitters' have been included as part of the ESI.†

Author contributions

Conceptualization: K. G.; investigation: K. G., J. L., S. S., and D. J.; supervision: D. T. G., D. J., and P. D.; visualization: K. G., S. S., J. L., and D. J.; writing – original draft: K. G., S. S., D. J., and D. T. G.; writing – review & editing: K. G., S. S., P. D.; D. J., and D. T. G.

Conflicts of interest

There are no conflicts to declare.

Acknowledgements

This work was supported by the Polish National Science Center, Poland (grants OPUS 2020/37/B/ST4/00017, 2022/45/B/ST5/03712 and HARMONIA 2018/30/M/ST5/00460). This project has received funding from the European Union's Horizon 2020 research and innovation programme under the Marie Skłodowka-Curie grant agreement no. 101007804. This research used resources from the GLiCID Computing Facility (Ligerien Group for Intensive Distributed Computing, **https://doi.org/10.60487/glicid**, Pays de la Loire, France). J. L. was the Doctoral Candidate in the Interdisciplinary Doctoral School at the Łódź University of Technology, Poland. We thank Joseph Milton for amending the manuscript.

Notes and references

1 K. Yamamoto, T. Harada, M. Nakazaki, T. Naka, Y. Kai, S. Harada and N. Kasai, *J. Am. Chem. Soc.*, 1983, **105**, 7171–7172.
2 I. R. Márquez, N. Fuentes, C. M. Cruz, V. Puente-Muñoz, L. Sotorrios, M. L. Marcos, D. Choquesillo-Lazarte, B. Biel, L. Crovetto, E. Gómez-Bengoa, M. T. González, R. Martin, J. M. Cuerva and A. G. Campaña, *Chem. Sci.*, 2017, **8**, 1068–1074.
3 K. Kawasumi, Q. Zhang, Y. Segawa, L. T. Scott and K. Itami, *Nat. Chem.*, 2013, **5**, 739–744.
4 S. K. Pedersen, K. Eriksen and M. Pittelkow, *Angew. Chem., Int. Ed.*, 2019, **58**, 18419–18423.
5 A. Caruso, M. A. Siegler and J. D. Tovar, *Angew. Chem., Int. Ed.*, 2010, **49**, 4213–4217.
6 R. E. Messersmith, S. Yadav, M. A. Siegler, H. Ottosson and J. D. Tovar, *J. Org. Chem.*, 2017, **82**, 13440–13448.
7 K. Kato, K. Takaba, S. Maki-Yonekura, N. Mitoma, Y. Nakanishi, T. Nishihara, T. Hatakeyama, T. Kawada, Y. Hijikata, J. Pirillo, L. T. Scott, K. Yonekura, Y. Segawa and K. Itami, *J. Am. Chem. Soc.*, 2021, **143**, 5465–5469.
8 J. Liu, S. Mishra, C. A. Pignedoli, D. Passerone, J. I. Urgel, A. Fabrizio, T. G. Lohr, J. Ma, H. Komber, M. Baumgarten, C. Corminboeuf, R. Berger, P. Ruffieux, K. Müllen, R. Fasel and X. Feng, *J. Am. Chem. Soc.*, 2019, **141**, 12011–12020.
9 M. Rickhaus, M. Mayor and M. Juríček, *Chem. Soc. Rev.*, 2017, **46**, 1643–1660.
10 S. Qiu, A. C. Valdivia, W. Zhuang, F.-F. Hung, C.-M. Che, J. Casado and J. Liu, *J. Am. Chem. Soc.*, 2024, **146**, 16161–16172.
11 C. M. Cruz, I. R. Márquez, I. F. A. Mariz, V. Blanco, C. Sánchez-Sánchez, J. M. Sobrado, J. A. Martín-Gago, J. M. Cuerva, E. Maçôas and A. G. Campaña, *Chem. Sci.*, 2018, **9**, 3917–3924.
12 R. Li, B. Ma, S. Li, C. Lu and P. An, *Chem. Sci.*, 2023, **14**, 8905–8913.
13 K. Górski, J. Mech-Piskorz, B. Leśniewska, O. Pietraszkiewicz and M. Pietraszkiewicz, *J. Org. Chem.*, 2020, **85**, 4672–4681.
14 K. Górski, J. Mech-Piskorz, K. Noworyta, B. Leśniewska and M. Pietraszkiewicz, *New J. Chem.*, 2018, **42**, 5844–5852.
15 M. Más-Montoya, L. Usea, A. E. Ferao, M. F. Montenegro, C. Ramírez de Arellano, A. Tárraga, J. N. Rodríguez-López and D. Curiel, *J. Org. Chem.*, 2016, **81**, 3296–3302.
16 T. Fujikawa, Y. Segawa and K. Itami, *J. Org. Chem.*, 2017, **82**, 7745–7749.
17 D. Tan, J. Dong, T. Ma, Q. Feng, S. Wang and D. Yang, *Angew. Chem., Int. Ed.*, 2023, **62**, e202304711.
18 M. Żyła, E. Gońka, P. J. Chmielewski, J. Cybińska and M. Stępień, *Chem. Sci.*, 2016, **7**, 286–294.
19 S. Stecko and D. T. Gryko, *JACS Au*, 2022, **2**, 1290–1305.
20 D. H. Friese, A. Mikhaylov, M. Krzeszewski, Y. M. Poronik, A. Rebane, K. Ruud and D. T. Gryko, *Chem.–Eur. J.*, 2015, **21**, 18364–18374.
21 M. Tasior, G. Clermont, M. Blanchard-Desce, D. Jacquemin and D. T. Gryko, *Chem.–Eur. J.*, 2019, **25**, 598–608.
22 Y. Ji, Z. Peng, B. Tong, J. Shi, J. Zhi and Y. Dong, *Dyes Pigm.*, 2017, **139**, 664–671.
23 K. Li, Y. Liu, Y. Li, Q. Feng, H. Hou and B. Z. Tang, *Chem. Sci.*, 2017, **8**, 7258–7267.
24 Y. Ma, Y. Zhang, L. Kong and J. Yang, *Molecules*, 2018, **23**, 3255.
25 B. Dereka and E. Vauthey, *Chem. Sci.*, 2017, **8**, 5057–5066.
26 J.-Y. Wu, C.-H. Yu, J.-J. Wen, C.-L. Chang and M. Leung, *Anal. Chem.*, 2016, **88**, 1195–1201.
27 M. Tasior, O. Vakuliuk, A. Wrzosek, V. I. Vullev, A. Szewczyk, D. Jacquemin and D. T. Gryko, *ACS Org. Inorg. Au*, 2024, **4**, 248–257.
28 J. Wang, Z. Chai, S. Liu, M. Fang, K. Chang, M. Han, L. Hong, H. Han, Q. Li and Z. Li, *Chem.–Eur. J.*, 2018, **24**, 18032–18042.
29 R. Domínguez, N. F. Montcada, P. de la Cruz, E. Palomares and F. Langa, *Chempluschem*, 2017, **82**, 1096–1104.
30 Y. Zhou, M. Zhang, J. Ye, H. Liu, K. Wang, Y. Yuan, Y.-Q. Du, C. Zhang, C.-J. Zheng and X.-H. Zhang, *Org. Electron.*, 2019, **65**, 110–115.
31 P. P. Abatti, N. O. Decarli, S. Gogoc, P. Data, I. H. Bechtold, E. Westphal and H. Gallardo, *ChemPlusChem*, 2023, **88**, e202300539.
32 M. Tasior, O. Vakuliuk, D. Koga, B. Koszarna, K. Górski, M. Grzybowski, Ł. Kielesiński, M. Krzeszewski and D. T. Gryko, *J. Org. Chem.*, 2020, **85**, 13529–13543.
33 M. Krzeszewski, Ł. Dobrzycki, A. L. Sobolewski, M. K. Cyrański and D. T. Gryko, *Chem. Sci.*, 2023, **14**, 2353–2360.

34 M. Krzeszewski, Ł. Dobrzycki, A. L. Sobolewski, M. K. Cyrański and D. T. Gryko, *Angew. Chem., Int. Ed.*, 2021, **133**, 15125–15132.
35 M. Tasior, P. Kowalczyk, M. Przybył, M. Czichy, P. Janasik, M. H. E. Bousquet, M. Łapkowski, M. Rammo, A. Rebane, D. Jacquemin and D. T. Gryko, *Chem. Sci.*, 2021, **12**, 15935–15946.
36 N. I. Petrenko, M. M. Kozlova, T. N. Gerasimova and J. Fluor, *Chem*, 1987, **36**, 93–98.
37 P. K. Gutch and J. Acharya, *Heterocycl. Commun.*, 2007, **13**, 393–396.
38 Y. R. Jorapur, G. Rajagopal, P. J. Saikia and R. R. Pal, *Tetrahedron Lett.*, 2008, **49**, 1495–1497.
39 Y. Lin, N. Li and Y. Cherng, *J. Heterocycl. Chem.*, 2014, **51**, 808–814.
40 M. Ghafarzadeh, E. S. Moghadam and F. Faraji, *J. Heterocycl. Chem.*, 2013, **50**, 754–757.
41 F. M. García-Valle, V. Tabernero, T. Cuenca, M. E. G. Mosquera and J. Cano, *Organometallics*, 2019, **38**, 894–904.
42 A. W. H. Wardrop, G. L. Sainsbury, J. M. Harrison and T. D. Inch, *J. Chem. Soc., Perkin Trans. 1*, 1976, **563**, 1279–1285.
43 W. Hu, F. Teng, H. Hu, S. Luo and Q. Zhu, *J. Org. Chem.*, 2019, **84**, 6524–6535.
44 D. Tsvelikhovsky and S. L. Buchwald, *J. Am. Chem. Soc.*, 2011, **133**, 14228–14231.
45 P. P. M. A. Dols, B. J. B. Folmer, H. Hamersma, C. W. Kuil, H. Lucas, L. Ollero, J. B. M. Rewinkel and P. H. H. Hermkens, *Bioorg. Med. Chem. Lett.*, 2008, **18**, 1461–1467.
46 E. A. Hallinan, T. J. Hagen, R. K. Husa, S. Tsymbalov, S. N. Rao, J. P. VanHoeck, M. F. Rafferty, A. Stapelfeld, M. A. Savage and M. Reichman, *J. Med. Chem.*, 1993, **36**, 3293–3299.
47 J. M. Klunder, K. D. Hargrave, M. West, E. Cullen, K. Pal, M. L. Behnke, S. R. Kapadia, D. W. McNeil, J. C. Wu, G. C. Chow and J. Adams, *J. Med. Chem.*, 1992, **35**, 1887–1897.
48 M. Binaschi, A. Boldetti, M. Gianni, C. A. Maggi, M. Gensini, M. Bigioni, M. Parlani, A. Giolitti, M. Fratelli, C. Valli, M. Terao and E. Garattini, *ACS Med. Chem. Lett.*, 2010, **1**, 411–415.
49 H. Umemiya, H. Fukasawa, M. Ebisawa, L. Eyrolles, E. Kawachi, G. Eisenmann, H. Gronemeyer, Y. Hashimoto, K. Shudo and H. Kagechika, *J. Med. Chem.*, 1997, **40**, 4222–4234.
50 T. A. Ban, M. Fujimori, W. M. Petrie, M. Ragheb and W. H. Wilson, *Int. Pharmacopsychiatr.*, 1982, **17**, 18–27.
51 Y. Ren, Y. Wang, S. Liu and K. Pan, *ChemCatChem*, 2014, **6**, 2985–2992.
52 A. Janiga, E. Glodkowska-Mrowka, T. Stoklosa and D. T. Gryko, *Asian J. Org. Chem.*, 2013, **2**, 411–415.
53 R. Stężycki, M. Grzybowski, G. Clermont, M. Blanchard-Desce and D. T. Gryko, *Chem.–Eur. J.*, 2016, **22**, 5198–5203.
54 K. Górski, J. Mech-Piskorz, B. Leśniewska, O. Pietraszkiewicz and M. Pietraszkiewicz, *J. Org. Chem.*, 2019, **84**, 11553–11561.
55 K. Górski, T. Ostojić, M. Banasiewicz, E. T. Ouellette, L. Grisanti and D. T. Gryko, *Chem.–Eur. J.*, 2023, **29**, e2022034.
56 M. Krzeszewski, B. Thorsted, J. Brewer and D. T. Gryko, *J. Org. Chem.*, 2014, **79**, 3119–3128.
57 K. Górski, D. Kusy, S. Ozaki, M. Banasiewicz, R. Valiev, S. R. Sahoo, K. Kamada, G. Baryshnikov and D. T. Gryko, *J. Mater. Chem. C*, 2024, **12**, 1980–1987.
58 B. Dereka, A. Rosspeintner, Z. Li, R. Liska and E. Vauthey, *J. Am. Chem. Soc.*, 2016, **138**, 4643–4649.
59 F. Terenziani, A. Painelli, C. Katan, M. Charlot and M. Blanchard-Desce, *J. Am. Chem. Soc.*, 2006, **128**, 15742–15755.
60 T. Kim, J. Kim, H. Mori, S. Park, M. Lim, A. Osuka and D. Kim, *Phys. Chem. Chem. Phys.*, 2017, **19**, 13970–13977.
61 K. Górski, I. Deperasińska, G. V. Baryshnikov, S. Ozaki, K. Kamada, H. Ågren and D. T. Gryko, *Org. Lett.*, 2021, **23**, 6770–6774.
62 Y. M. Poronik, G. V. Baryshnikov, I. Deperasińska, E. M. Espinoza, J. A. Clark, H. Ågren, D. T. Gryko and V. I. Vullev, *Commun. Chem.*, 2020, **3**, 190.
63 A. Janiga, D. Bednarska, B. Thorsted, J. Brewer and D. T. Gryko, *Org. Biomol. Chem.*, 2014, **12**, 2874–2881.
64 K. Górski, K. Noworyta and J. Mech-Piskorz, *RSC Adv.*, 2020, **10**, 42363–42377.
65 B. Golec, A. Gorski, R. P. Thummel, M. Sierakowski and J. Waluk, *Photochem. Photobiol. Sci.*, 2023, **22**, 333–344.
66 J.-H. Lee, C.-H. Chen, P.-H. Lee, H.-Y. Lin, M. Leung, T.-L. Chiu and C.-F. Lin, *J. Mater. Chem. C*, 2019, **7**, 5874–5888.
67 G. Meng, D. Zhang, J. Wei, Y. Zhang, T. Huang, Z. Liu, C. Yin, X. Hong, X. Wang, X. Zeng, D. Yang, D. Ma, G. Li and L. Duan, *Chem. Sci.*, 2022, **13**, 5622–5630.
68 X. Li, J. Zhang, Z. Zhao, L. Wang, H. Yang, Q. Chang, N. Jiang, Z. Liu, Z. Bian, W. Liu, Z. Lu and C. Huang, *Adv. Mater.*, 2018, **30**, 1705005.
69 J. Lee, H. F. Chen, T. Batagoda, C. Coburn, P. I. Djurovich, M. E. Thompson and S. R. Forrest, *Nat. Mater.*, 2016, **15**, 92–98.
70 S. Nam, J. W. Kim, H. J. Bae, Y. M. Maruyama, D. Jeong, J. Kim, J. S. Kim, W. Son, H. Jeong, J. Lee, S. Ihn and H. Choi, *Adv. Sci.*, 2021, **8**, 2100586.
71 X. Cai and S. Su, *Adv. Funct. Mater.*, 2018, **28**, 1802558.
72 S. Izawa, M. Morimoto, K. Fujimoto, K. Banno, Y. Majima, M. Takahashi, S. Naka and M. Hiramoto, *Nat. Commun.*, 2023, **14**, 5494.